Structural modifications of boron carbide irradiated by swift heavy ions

Y. Pipon, G. Victor, N. Moncoffre, G. Gutierrez, S. Miro, T. Douillard, O. Rapaud, N. Pradeilles, P. Sainsot, N. Toulhoat, et al.

Journal of Nuclear Materials 546 (2021) 152737

Contents lists available at ScienceDirect

Journal of Nuclear Materials

journal homepage: www.elsevier.com/locate/jnucmat

Structural modifications of boron carbide irradiated by swift heavy ions

Y. Pipon[a,b,*], G. Victor[a], N. Moncoffre[a], G. Gutierrez[c], S. Miro[d], T. Douillard[e], O. Rapaud[f], N. Pradeilles[f], P. Sainsot[g], N. Toulhoat[a,c], M. Toulemonde[h]

[a] Univ Lyon, Univ Claude Bernard Lyon 1, CNRS/IN2P3, IP2I Lyon, UMR 5822, F-69622, Villeurbanne, France
[b] Univ Lyon, Univ Claude Bernard Lyon 1, IUT Lyon-1, Département chimie, F-69622, LYON, France
[c] Den-Service de Recherches de Métallurgie Physique (SRMP), Laboratoire JANNUS, CEA, Université Paris-Saclay, F-91191 Gif-sur-Yvette, France
[d] CEA Marcoule DEN/DTCD/SECM/LMPA, Atalante, 30207 Bagnols-sur-Cèze, France
[e] Univ Lyon, INSA Lyon, CNRS, MATEIS - UMR 5510, F-69621, LYON, France
[f] Univ. Limoges, CNRS, IRCER, UMR 7315, F-87000 Limoges, France
[g] Univ Lyon, INSA-Lyon, CNRS UMR5259, LaMCoS, F-69621, France
[h] ENSICAEN, CNRS, CEA, CIMAP, GANIL, Caen, France

ARTICLE INFO

Article history:
Received 11 September 2020
Revised 13 December 2020
Accepted 14 December 2020
Available online 26 December 2020

Keywords:
Structural modification
Swift heavy ion irradiation
Boron carbide
Raman spectroscopy
Electron microscopy

ABSTRACT

Boron carbide (B_4C) behavior under irradiation is widely studied in order to predict the lifetime of this material in future (Generation IV) nuclear fission reactors. This paper is focused on the effects of high electronic stopping powers (S_e) on B_4C structure modifications. Sintered B_4C samples were irradiated at room temperature with swift heavy ions (between 0.5 and 3 MeV·u^{-1}) corresponding to S_e values in the 4.1 to 15.4 keV·nm^{-1} range at the sample surface. In order to investigate the structural changes as a function of depth, transmission electron microscopy and Raman mapping were performed on the irradiated samples along the path of the incident ions. For the highest S_e values, damage results in the creation of large hillocks at the sample surface along with the amorphization of the bulk. These results are explained, in the frame of the inelastic thermal spike model, by local melting in latent tracks that are created only when irradiations are performed above a S_e threshold evaluated at around 9 keV nm^{-1}.

1. Introduction

The Generation IV International Forum (GIF), started in 2000 with thirteen countries, selected six concepts of future nuclear reactors with ambitious goals among them sustainability, safety and reliability [1]. In France, some fundamental research is focused on the Sodium-Fast Reactor (SFR) concept, in particular because of a long experience on previous plants with the same technology: Rapsodie (1967–1983), Phenix (1973–2009) and Superphenix (1985–1997) [2]. A program named ASTRID (Advanced Sodium Technological Reactor for Industrial Demonstration) [3] was conducted between 2010 and 2019. It aimed at designing a SFR demonstrator with a power of 600 MWe and included a R&D program on the closure of the fuel cycle (manufacturing, reprocessing). This program has been designed in prevision of the SFR technology deployment for 2060. The design and the materials for ASTRID have been fixed but the aging of the materials has to be fully explored in order to predict their lifetime in severe conditions. For instance, boron carbide (B_4C) will be used in control rods and will be exposed to: (i) temperature up to 1100 K and, (ii) neutron irradiation which can induce up to 200 displacements per atom (dpa). This irradiation also leads to other effects such as the swelling of the pellets through helium production via the following main neutron capture reaction:

$$^{10}B + n \rightarrow \alpha(1.47\ MeV) + {}^{7}Li(0.84MeV) + \gamma(0.48\ MeV)$$

Nowadays, in Pressurized Water Reactors (PWR) control rods, boron carbide is already used as neutron absorber due to the very high value of thermal neutron absorption cross section of ^{10}B (3840 barns from ENDF -*Evaluated Nuclear Data File*- database). At higher energies, this cross section decreases, but less than for other potential absorbers, which makes boron carbide a promising absorber for SFR. From literature data [4–10], main results obtained on the B_4C behavior under irradiation come from integral experiences (irradiation in reactor). For instance, visual examination of boron carbide pellets after irradiation in Phenix reactor has

* Corresponding author at: Université de Lyon, UCBL, IP2I, Campus LyonTech La Doua, 4 rue Enrico Fermi, 69622 Villeurbanne cedex, France.
E-mail address: y.pipon@ipnl.in2p3.fr (Y. Pipon).

https://doi.org/10.1016/j.jnucmat.2020.152737
0022-3115/

shown a lot of crackings resulting from the coupling of a bad thermal conductivity (30 $W{\cdot}m^{-1}{\cdot}K^{-1}$ at room temperature) decreasing with temperature and an intense radial thermal gradient (800 $K{\cdot}cm^{-1}$) [11]. Nevertheless, no amorphization of the structure has ever been observed, which explains that B_4C is considered to be radiation resistant even if the reasons of this resistance remain to be clarified. The difficulties arise partially from the complex crystallographic structure of boron carbide. It belongs to the $R\bar{3}m$ space group (rhombohedral symmetry). The B_4C unit (elementary) cell is composed of 15 atoms: an icosahedron of twelve atoms placed at each vertice of the cell and three atoms forming a central chain linking two icosahedra along the [111] axis of the rhombohedron. The assignment of boron and carbon atom positions in the lattice is a challenging task, as many polytypes exist. Most studies (see for instance [12–13] for a theoretical study and an experimental one) agree that the most stable structure is $(B_{11}C^{p})CBC$: an icosahedron composed of eleven boron atoms and one carbon atom at the polar site of the icosahedron (corresponding to the atom linked to another icosahedron) and a linear C-B-C chain.

During reactor operation, it is known that neutrons, especially thermal ones, induce mainly atomic displacements. Heavy ion irradiation at low energy is usually considered to simulate this type of damage. In the literature, Gosset et al. [14–15] have shown that 4 MeV Au irradiation, at Room Temperature (RT), leads to B_4C amorphization at around 4 dpa. The amorphization is somewhat influenced by the insertion of Au ions in the B_4C structure which could lower the amorphization threshold. This was put in evidence by the work of Victor et al. [16] who have shown that amorphization only induced by ballistic collisions (with almost no insertion of ions in the structure) starts only around 7.5 dpa. However, if we consider the whole neutron spectrum during reactor operation, the fastest neutrons can reach up to 10 MeV energy, and their interactions with matter can induce electronic excitations whose effects in B_4C have been very few studied. Some irradiations on boron carbide samples have been performed with electrons [17–18]. Amorphization has been observed with a 2 MeV electron irradiation at a very high fluence of 1.3×10^{24} $e{\cdot}cm^{-2}$ and at 106 K. Maruyama et al. [19] have also observed B_4C amorphization after irradiation with 15 MeV He ions at fluences up to 2×10^{17} $ions{\cdot}cm^{-2}$. At last, Mirzayev et al. [20] reported B_4C partial amorphization (62%) under gamma irradiation with an irradiation dose of 194.4 KGy.

Hence, we aim at studying the structural modifications under irradiation conditions enhancing strongly the electronic excitations. For that purpose, we perform several irradiation experiments of B_4C samples with Swift Heavy Ions (SHI). First preliminary results on the B_4C structure evolution after irradiation with 100 MeV iodine ions were presented in a previous paper [21] in which damage was put in evidence by Raman analysis but only at the sample surface. The originality of this paper is that: (i) several irradiation conditions were used in order to vary the electronic stopping power (S_e) values at the surface, (ii) the Raman analysis was performed all along the incident ion range, in order to determine the structure modifications as a function of the electronic stopping power evolution, (iii) the iTS (inelastic Thermal Spike) model was applied in order to explain the amorphization of the samples.

2. Material and methods

This section provides information on the preparation of the boron carbide samples from the powder to the thin foils, on the irradiation conditions and on the characterization performed on the irradiated samples.

2.1. Boron carbide sample preparation

The powder sintering was carried out from a commercial (H.C. Starck) submicrometric powder HD 20 of boron carbide with a purity of 99.5%, an average diameter of 400 nm and a specific area of 24 $m^2{\cdot}g^{-1}$ [22–23]. Powder has been densified without sintering additives using SPS facility (Fuji-Syntex, Dr Sinter 825, Japan) under dynamic vacuum. For each sample the heating rate (200 K min^{-1}), the dwell time (5 min) and the maximal temperature (2123 K) were fixed. A uniaxial pressure of 75 MPa was applied upon heating and released when temperature reached 873 K at the end of the heat treatment [24]. These conditions allow obtaining dense samples (more than 99% of the theoretical relative density) with a grain size distribution centered at around 650 nm. The samples are 2 mm length and 10 mm diameter cylindrical pellets. Their surfaces were then polished in order to obtain a roughness lower than 30 nm. The last preparation stage consisted of two successive annealing: first at 1273 K during 10 h in order to desorb impurities from the surface, and then at 1673 K during 3 h in an induction furnace in order to remove the major part of the polishing defects. The annealing was performed under high vacuum ($\approx10^{-7}$ mbar) to prevent any oxidation of the samples.

2.2. Irradiation conditions

Irradiation experiments were performed at the 15 MV ALTO Tandem accelerator facility, at the Nuclear Physics Institute (IPN, Orsay, France) with heavy ions: sulfur and iodine ions (any atom consisting of more than twenty nucleons is considered as “heavy”) at the same 9+ charge. We used an experimental irradiation chamber described in a previous paper [25] to maintain the pressure at around 10^{-6} mbar. The irradiation conditions are summarized in Table 1.

All irradiations were performed at RT with the same flux (around 1.5×10^{11} $at{\cdot}cm^{-2}{\cdot}s^{-1}$) and with fluences of the same order of magnitude (5×10^{15} $at{\cdot}cm^{-2}$ for sulfur ions irradiation and iodine ions irradiation at 100 MeV and 3×10^{15} $at{\cdot}cm^{-2}$ for iodine irradiation at 60 MeV). The mean ion ranges, the electronic and nuclear stopping powers (S_e and S_n) and the maximum of dpa were calculated thanks to the SRIM-2013 software [26] in the full damage cascades mode considering a boron carbide density of 2.5 $g{\cdot}cm^{-3}$ and displacement energies of 25 eV and 28 eV for Boron and Carbon respectively (default values in SRIM). We can see from Table 1 that the S_n values remain always low (between 0.003 and 0.12 $keV{\cdot}nm^{-1}$) at the surface. In particular, the sulfur ion irradiation corresponds to a pure electronic regime because of the high velocity of the incident ions (3.1 $MeV{\cdot}u^{-1}$) and a very high value of the S_e/S_n ratio. However, the corresponding S_e value (4.1 $keV{\cdot}nm^{-1}$) itself is rather low. This value is comparable (even if a little higher) to the recoil ion energy induced by the fastest neutrons during reactor operation (around 2 $keV{\cdot}nm^{-1}$ for carbon atom recoils after an impact with a 10 MeV neutron). iodine ion irradiations correspond to a mixed irradiation regime if we refer to the velocity criterion estimated between 50 $keV{\cdot}u^{-1}$ and 1 $MeV{\cdot}u^{-1}$ in the literature [27]. Therefore, nuclear collisions and electronic excitations should both play a role for the material damaging. The corresponding S_e values at the surface (12.8 and 15.4 $keV{\cdot}nm^{-1}$) are high. If the ion-induced excitation is sufficiently intense, permanent damage should be created in the material and latent tracks can be observed at the surface. With SHI, these tracks appear only when a S_e threshold is exceeded [28] but this threshold value remains unknown for B_4C. The number of dpa at the boron carbide surface calculated with SRIM is near null for sulfur ions (0.008 dpa) and very low but not negligible for iodine ions (below 0.2 dpa). It has to be noted that no defect has been observed by Victor et al. [16] as long as the damage was below 0.5

Table 1
Summary of the main parameters corresponding to the irradiation conditions by sulfur and iodine ions in B_4C. Range of ions, maximum dpa value, electronic and nuclear stopping powers (S_e and S_n) were calculated with SRIM software. The same flux (1.5×10^{11} at·cm^{-2}·s^{-1}) and fluences of the same order of magnitude (5×10^{15} at·cm^{-2} for sulfur ions irradiation and iodine ions irradiation at 100 MeV and 3×10^{15} at cm^{-2} for iodine irradiation at 60 MeV) were performed.

Ions	Energy (MeV)	Range of ions (μm)	Max dpa	Velocity (MeV u^{-1})	S_e (keV nm^{-1}) *surface*	S_n (keV nm^{-1}) *surface*	{S_e / S_n} *surface*
^{32}S	100	21.7	1.2	3.1	4.1	0.003	1370
^{127}I	60	8.5	2.5	0.5	12.8	0.12	100
^{127}I	100	11.2	4.1	0.8	15.4	0.07	220

dpa. At last, we can calculate with SRIM that the maximum dpa value is 4.1 dpa at a depth of 11.2 μm for the 100 MeV iodine ions, 2.5 dpa at a depth of 8.5 μm for the 60 MeV iodine ions and, 1.2 dpa at a depth of 21.7 μm for the 100 MeV sulfur ions.

2.3. Sample characterization

Raman spectroscopy is a very appropriate technique to study the structural modifications induced by ion irradiation in nuclear ceramics [29]. We have performed two kinds of analyses: (i) line mapping at the surface of all irradiated samples; (ii) line mapping on the cross-section of some irradiated samples, which is possible because the ion ranges are of the order of magnitude of a few micrometers. This second type of analysis allows following damage evolution as a function of depth, from the surface down to the end of the irradiated zone. In order to perform Raman spectroscopy along the incident ion path, B_4C samples were cut perpendicularly to the surface. Half of the sample was sticked on a metallic base and mounted in epoxy resin (EpoFix TM) before polishing. Raman characterizations were carried out with a Renishaw Invia Reflex device equipped with a Leica DM2500 microscope (x100 objective) at the JANNUS laboratory at Saclay. Raman scattering measurements were performed using the 532 nm wavelength of a frequency-doubled Nd–YAG laser with an output power of around 1 mW to avoid sample heating. The nominal spot size was estimated to be around 0.8 μm. The Raman spectrometer was calibrated by using silicon monocrystalline samples. Raman analysis was then performed in a line mapping mode. A Raman spectrum was recorded every 100 nm from the surface of the cross-section until a depth which exceeds the ion projected range of the irradiation beam.

In order to put in evidence irradiation induced morphological modifications at the sample surface, scanning electron microscope (SEM) observations were performed at the cTμ plateform (Lyon University, France) with an acceleration voltage of 5 kV and a vacuum better than 7×10^{-5} mbar ($< 5 \times 10^{-5}$ Torr). The surface roughness was studied by optical interferometry with a Neox 3D interferometer of Sensofar. The measurements were carried out at the *Laboratoire de Mécanique des Contacts et des Structures* (LaMCoS, INSA Lyon, France).

From the B_4C pellets, thin foils were prepared by the Focused Ion Beam (FIB) technique at the *center Lyonnais de Microscopie* (CLYM, INSA Lyon, France). These TEM thin sections were made using a FIB / SEM workstation (NVision 40; Carl Zeiss Microscopy GmbH, Oberkochen, Germany) combining a SIINT zeta FIB column (Seiko Instruments Inc. NanoTechnology, Japan) with a Gemini I column. The NVision 40 plateform is also equipped with a multi-nozzle SIINT Gas Injection System (GIS). The *in situ* lift-out of the thin foils from pre-selected sections of irradiated site was carried out with a Cartesian nano-robotic manipulator (Klocke Nanotechnik GmbH, Aachen, Germany). FIB milling was done perpendicular to the direction of (iodine or sulfur) ion irradiation. To minimize the curtain effect introduced by the gallium ion beam milling and to protect the sample surface from implantation, we have first performed an *in situ* ion beam induced deposition over the area of interest with tungsten carboxyl $W(CO)_6$ as a precursor gas (sputter-resistant layer of about 1 μm). Trenches were milled to enable the extraction of 1–2 μm thick lamellas. They were then transferred (using the manipulator) and glued (using the GIS) onto a TEM copper grid for further thinning. In this work, settings for 30 kV ion accelerating voltage with decreasing beam currents (700 pA to 40 pA) and probe sizes were used to reach a suitable foil thickness for TEM analysis (around 150 nm). At each step, milling was carried-out using an adjusted grazing incidence to compensate for the ion beam tails in order to achieve near parallel foil top and bottom surfaces over a large zone. Finally, to reduce the expected amorphous layer due to the 30 keV Ga^+ ion beam, we performed a final low-kV ion polishing at 2 kV with a 50 pA current. Microstructural examination in the direction normal to the surface (*i.e.* from the irradiated surface to the bulk) was carried out using a field emission high-resolution TEM (JEOL JEM-2010 FEG) and a LaB_6 TEM (JEM-2100 LaB_6). We performed annular dark-field (ADF) images in scanning electron microscopy transmission (STEM) mode. Contrasts in ADF images are sensitive to both the atomic number of atoms in the sample (Z-contrast component) and crystallographic orientation (crystalline phase component).

We also used the Selected Area Electron Diffraction (SAED) technique to study the crystalline state (amorphous or crystalline). The operating mode of the SAED method consists in illuminating a sample area with a parallel beam so that the transmitted wave and the diffracted waves are focused in the focal plane of the objective. The extent of the analyzed area is determined by the diameter of a field limiting aperture. In our experiments, this circular area was set to about 545 nm. The appearance of the diffraction pattern is related to the nature of the phases in the specimen. If the material is amorphous, the diffraction pattern consists of a series of diffuse concentric rings instead of spots for crystalline phase.

3. Results

We will present first the results obtained at the surface and then the results obtained at different depths of the samples.

3.1. Surface analyses of irradiated samples: experimental results

The present section will first present the experimental results obtained by Raman spectroscopy and SEM on a virgin sample and on the sulfur and iodine irradiated samples.

Fig. 1 shows the Raman spectra obtained at the surface of the B_4C virgin sample (Fig. 1.a) and of the B_4C irradiated samples with sulfur ions (Fig. 1.b) and with iodine ions (Fig. 1.c and 1.d).

Let us first consider the virgin spectrum (Fig. 1.a). The Raman shift values of the main bands are localized between 200 cm^{-1} and 1200 cm^{-1}. However, the bands between 200 cm^{-1} and 400 cm^{-1} will not be discussed in this paper since some authors in the literature suggest that the corresponding modes do not belong to the boron carbide structure but to a high density of states of disorder-activated acoustic phonons [30]. The other bands can be assigned to vibrational modes among the 30 ones existing for boron carbide. *Ab initio* DFT (Density functional Theory) calculations from

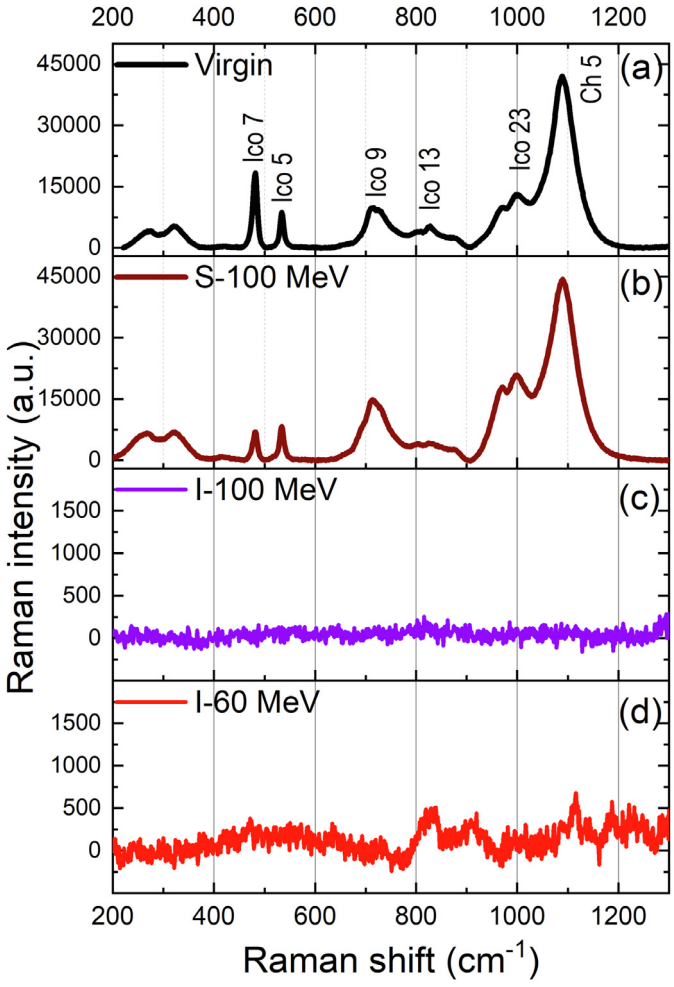

Fig. 1. *Raman spectra at the surface of the virgin sample (a) and of the samples irradiated by 100 MeV sulfur ions at a fluence of* 5×10^{15} *ions·cm*$^{-2}$ *(b), 100 MeV iodine ions at a fluence of* 5×10^{15} *ions·cm*$^{-2}$ *(c) and 60 MeV iodine ions at a fluence of* 3×10^{15} *ions·cm*$^{-2}$ *(d).*

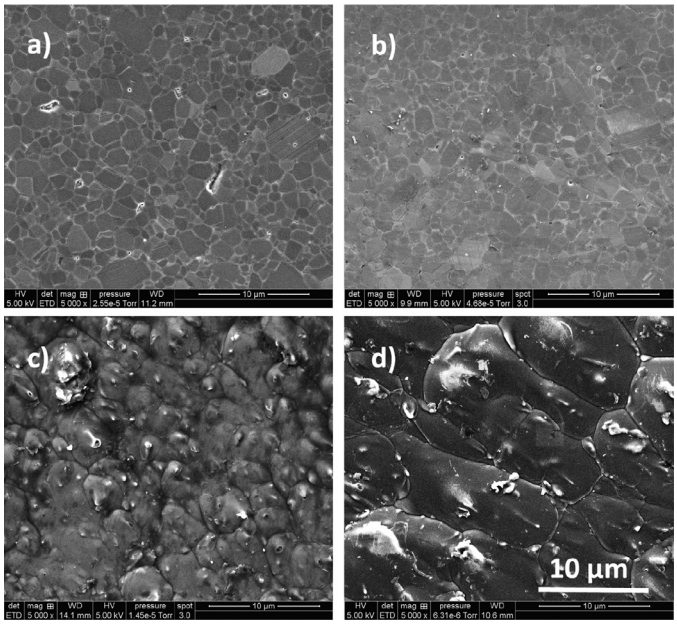

Fig. 2. *SEM images of the* B_4C *sample surface before irradiation (a), after irradiation with 100 MeV sulfur ions at a fluence of* 5×10^{15} *ions·cm*$^{-2}$ *(b), 60 MeV and 100 MeV iodine ions at a fluence of* 3×10^{15} *ions·cm*$^{-2}$ *and* 5×10^{15} *ions·cm*$^{-2}$ *respectively (c) and (d).*

Jay [31] show that these vibrational modes are shared between 6 modes for the linear chain and 24 modes for the icosahedron. This author has also computed a theoretical Raman spectrum that is very close to our virgin spectrum. We therefore labeled the main bands according to the names given by Jay. The bands labeled ICO are due to a vibrational mode involving atoms placed into an icosahedron and the bands labeled CH are due to a vibrational mode of the linear chain.

We can identify six main bands on three regions of interest displayed in Fig. 1.a:

- Two quasi-degenerate harmonic E_g modes at 480 and 535 cm^{-1} (labeled respectively ICO 7 and ICO 5) which are the fingerprints of B_4C. ICO 7 is a pseudo-rotation of the linear chain (vibration involving chain and icosahedra) and ICO 5 corresponds to a libration of each icosahedron;
- A first widespread band gathering five modes between 600 and 900 cm^{-1} corresponding to intra-icosahedra vibrations. The two most intense bands are displayed at 720 cm^{-1} (ICO 9) and at 825 cm^{-1} (ICO 13);
- A second widespread band gathering also five modes between 900 and 1100 cm^{-1}. The most intense band is displayed at 1090 cm^{-1} (CH 5) and the second one at 1000 cm^{-1} (ICO 23).

The Raman spectrum of the irradiated sample with sulfur ions (Fig. 1.b) is very similar to that of the virgin sample. The width and position of all bands of interest remain constant. However, the band intensity values change after irradiation. In particular, the ratio of ICO 7 over ICO 5 is very different from that of the virgin spectrum. One possible explanation is a grain orientation effect. Indeed this behavior was also observed when recording a single spectrum at different locations of the virgin sample surface (see supplementary material). Therefore, most probably, the irradiation with sulfur ions has no (or almost no) apparent impact on the structure.

On the contrary, the 60 MeV and 100 MeV iodine irradiated sample spectra (Fig. 1.c and 1.d) are flat or nearly flat with the complete disappearance of ICO 5 and ICO 7, suggesting that the samples have undergone structural changes such as an amorphization process. Pallier et al. [32] have analyzed by Raman amorphous boron carbide elaborated by CVD. They observe a first intense broad band between 400 cm^{-1} and 800 cm^{-1} similar to the one seen at the same Raman shifts in Fig. 1.d. They also evidenced a second broad band between 900 and 1300 cm^{-1}. At these wavenumbers, we can only observe some tiny peaks in Fig. 1.d which can be some bands. Pallier attributes these bands to the presence of some distorted icosahedra. We can therefore assume that irradiation with 60 MeV iodine ions has destroyed almost entirely the atomic order.

The drastic structural changes suggested by the Raman spectra are corroborated by the SEM images obtained at the sample surface and presented in Fig. 2 for the virgin sample (Fig. 2.a) and the irradiated ones (Fig 2.b to 2.d).

Same magnification has been used to easily compare each SEM image on Fig. 2. First, we can notice that the virgin sample surface and the sulfur irradiated one are rather similar, without noticeable modifications of the grain sizes nor the grain boundaries (Fig. 2 (a, b)). Fig. 2.c and 2.d present the iodine irradiated sample surfaces. These two figures show a kind of “magmatic” surface aspect, which is especially notable for the 100 MeV irradiation energy. It suggests a growing and a swelling of the grains. The grain boundaries are not visible anymore and some “hillocks” replace the grains. For the sample irradiated with 60 MeV iodine ions, these “hillocks” are about two or three times larger than the grains of the boron car-

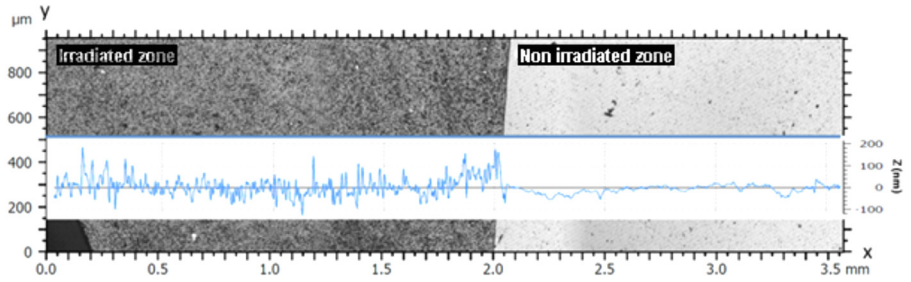

Fig. 3. *Surface roughness (Z in nm) measured by optical interferometry at the surface of the B_4C sample irradiated with 60 MeV at a fluence of 3×10^{15} ions·cm^{-2}. (For interpretation of the references to colour in this figure legend, the reader is referred to the web version of this article.)*

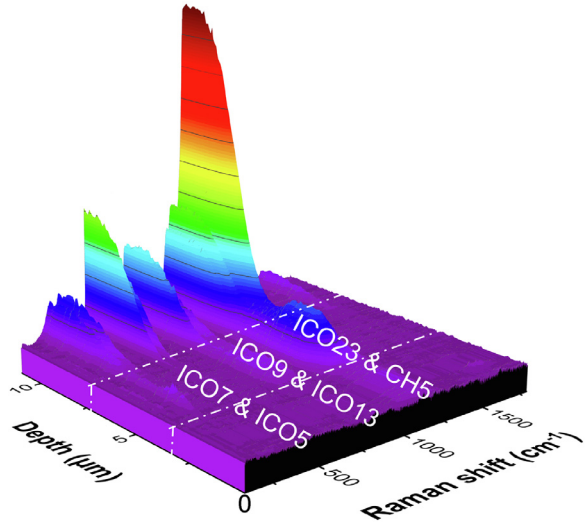

Fig. 4. *Raman depth line scan obtained on a B_4C sample irradiated with 60 MeV iodine ions at a fluence of 3×10^{15} ions·cm^{-2}. Three main zones are identified and delimited by white dashed lines.*

bide virgin sample. For the sample irradiated with 100 MeV iodine ions, they are ten times larger. The induced roughness is very important. It is put in evidence in Fig. 3, which displays the results of optical interferometry analyses performed on a sample irradiated with 60 MeV iodine ions. Due to the sample fixing brackets, a small part of the sample is masked from the ion beam during irradiation. This allows comparing the irradiated zone (left part of Fig. 3) and the non irradiated region (right part of Fig. 3) on the same sample. The roughness induced by irradiation is shown to increase from around 30 nm to a mean value of 200 nm (maximum value of 500 nm). This means that the formation of hillocks observed in Fig. 2 induces an important swelling of the samples surface.

It is important to remind that a major drawback of the Raman spectra recorded at the surface is that the signal is originating from an average volume, inside which the stopping power value is decreasing with respect to the depth. That is the reason why the next section deals with the study of the damage evolution in function of the sample depth with more accuracy.

3.2. In-depth analysis: damage evolution in function of the sample depth

This section presents a comparison of the Raman and TEM analyses results obtained on iodine irradiated samples. We will focus on the sample irradiated with the 60 MeV iodine ions. First, we have studied the evolution of the B_4C damage as a function of depth thanks to Raman mapping on cross-sections of the irradiated samples. The results are presented in Fig. 4 in three dimensions, the z scale being the intensity of the Raman modes. The 0 µm value represents the border of the cut sample, *i.e.* the entrance side of the iodine ions. Three main zones can be observed. They have been delimited in Fig. 4 by dashed white lines.

In the first three microns, the material seems to be completely amorphized since no peak can be seen. This result is in agreement with the surface analyses by Raman spectroscopy (see Fig. 1d). At a depth between 3 µm and 7.5 µm, a slight increase of the different mode intensities is observed. This suggests that the zone is not anymore amorphized but not fully crystalline either. Then a brief decrease (clearly observed on ICO 23 and CH 5) is seen at a depth around 7.5 µm. This corresponds to the Bragg peak where ballistic damage is at its maximum just before the iodine ions stop in B_4C (at around 8.5 µm). Beyond 9 µm, corresponding roughly to the non-irradiated zone, the B_4C structure is completely recovered as the Raman mode intensity does not evolve anymore.

In order to go further in the irradiation effect analysis, thin electron-transparent sections were prepared by Focused Ion Beam and then analyzed by TEM. A detailed analysis of the material structure evolution was performed thanks to a line scan of SAED (Selected Area Electron Diffraction) patterns. Fig. 5 presents TEM images obtained from the 60 MeV irradiated sample.

In Fig. 5, color circles depict the successive positions of the aperture used for SAED. The bright parts visible on the top and on the left of the lamella are *in situ* deposition of tungsten performed for the FIB preparation purpose. The bar across the patterns is the "beam stop" used to cover the bright central beam spot so that the more diffuse rings can be captured as a digital image.

Three zones, highlighted by different colors, can be distinguished from Fig. 5:

(i) From the surface down to a depth of around 2.2 µm. No grain is visible from Fig. 5a and SAED patterns (Fig. 5b) are typical of a totally amorphous material (two diffuse concentric rings); The first SAED pattern in Fig. 5c (between 2.2 and 2.7 µm) displays a mixture of amorphous and crystalline phases corresponding clearly to the amorphous / crystalline transition region. This transition was observed roughly before 3 µm by Raman spectroscopy;

(ii) From 2.2 µm down to a depth of around 6 µm. Fig. 5a displays a mixed region with some grains in this region. SAED patterns (Fig. 5c) are showing the coexistence of an amorphous phase with a crystalline phase (overlap of an amorphous diffraction pattern with a classic spot diffraction pattern). We can also see that the amorphous component decreases with depth and so with S_e;

(iii) From 6 µm down to a depth of around 7.5 µm (maximum probed depth). All grains are clearly visible in Fig. 5a and a full crystalline material is observed from the SAED patterns (Fig. 5d) because of the random reflections (*i.e.* no grain is oriented with a zone axis pattern parallel to the electron beam). This information would not be available by using Raman spectroscopy.

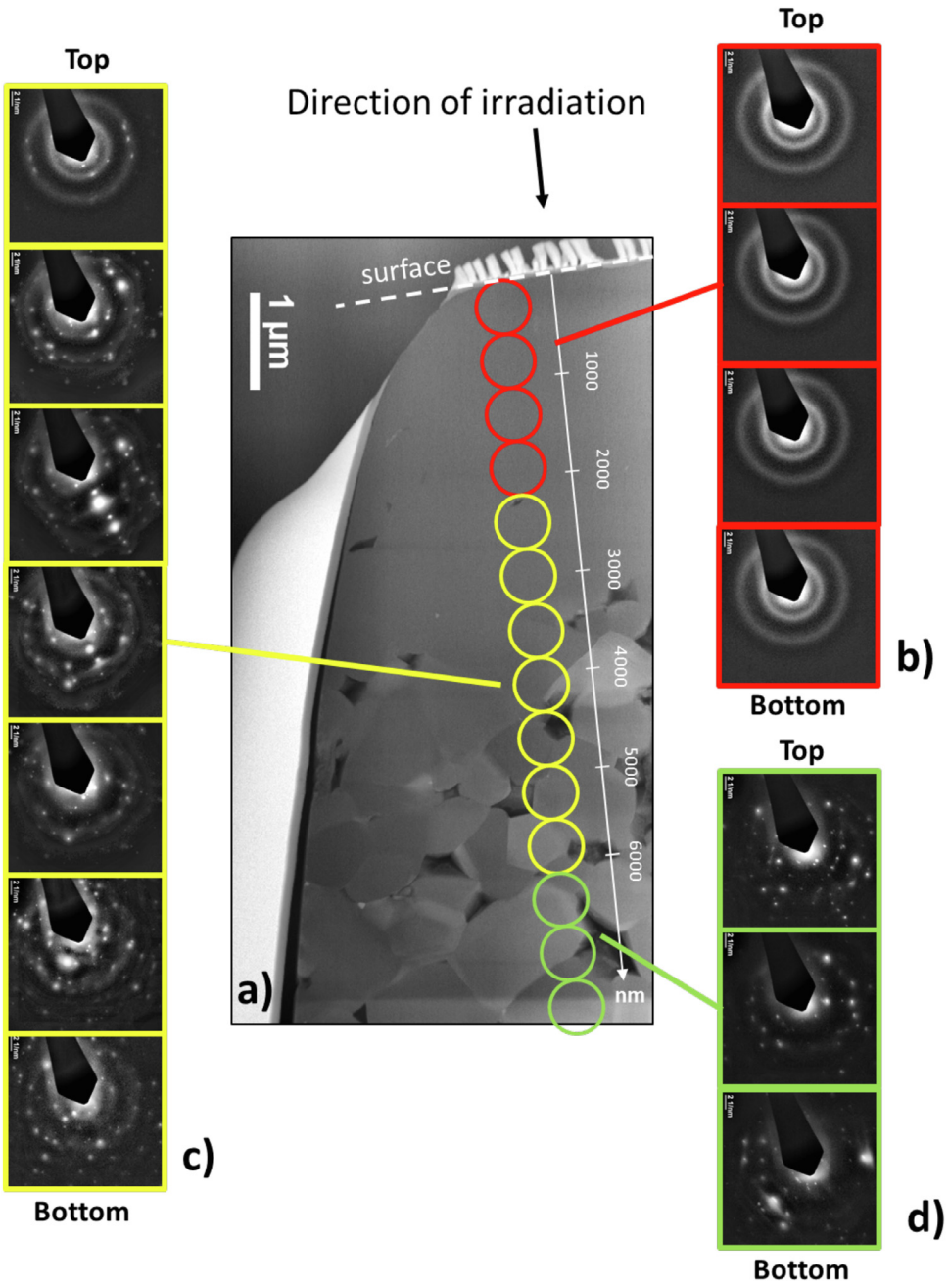

Fig. 5. *(a) is a STEM-ADF image of a B_4C thin foil from a sample irradiated with 60 MeV iodine ions at a fluence of 3×10^{15} ions·cm^{-2}. (b) to (d) are SAED patterns taken from the irradiated surface to the bulk. Each color circle indicates a position of the aperture used for SAED. Three different colors are used to distinguish the different zones. Contrast Limited Adaptive Histogram Equalization was done the same way on each SAED patterns to better apprehend the presence of diffuse rings.*

At last, the region containing the maximum damage peak (around 8.5 µm as calculated by SRIM) is not observed by TEM as it was not possible to obtain a thin section large enough to probe this depth.

3.3. Conclusions on the experimental results

The Raman spectroscopy and the SEM performed at the surface of the irradiated samples show that: (i) iodine ions induce amorphization; (ii) sulfur ions at 100 MeV do not induce any significant changes.

Damage induced by the iodine ions at different depths of the samples has been probed by Raman and by TEM. The combination of these analysis methods allows to distinguish the nature of three different regions: (i) fully amorphized, (ii) mix with amorphization and crystalline areas and (iii) fully crystalline. These results suggest the existence of a stopping power threshold, below which amorphization is not complete.

4. The iTS (inelastic thermal spike) model for data description

4.1. Model formalism

The thermal spike effect was first raised in 1959 by Silk and Barnes to explain the track formation induced by fission fragments in mica [33]. This is a two-step process where energetic incident ions transmit, at first, their energy to the electrons of a material. Secondly, this energy is transferred to the atoms by an electron-phonon coupling. When the deposited energy exceeds the melting energy, the irradiated material becomes sensitive to the electronic

energy loss process and can undergo structural modifications (formation of point defects, annealing of defects, crystallization, amorphization, sputtering ...). The inelastic thermal spike (iTS) model in insulators was fully described by Toulemonde et al. in several papers (see for instance [34]). It includes two interacting sub-systems: the electrons described within the quasi-free electron gas model and the atoms following the Debye model. Each sub-system is characterized by thermodynamic parameters: mainly the temperature "T", the specific heat "C" and the thermal conductivity "K". The electronic (e) and atomic (a) temperatures are governed by the following set of coupled equations (Eq. (1) and Eq. (2)) which describe the thermal energy deposited in a cylindrical slice whose radius r is ranging between r and $r + dr/2$ with respect to time (t).

$$C_e(T_e)\frac{\partial T_e}{\partial t} = \frac{1}{r}\frac{\partial}{\partial r}\left[rK_e(T_e)\frac{\partial T_e}{\partial r}\right] - g(T_e - T_a) + A(r,t) \quad (1)$$

$$C_a(T_a)\frac{\partial T_a}{\partial t} = \frac{1}{r}\frac{\partial}{\partial r}\left[rK_a(T_a)\frac{\partial T_a}{\partial r}\right] - g(T_e - T_a) + B(r,t) \quad (2)$$

The C_a (lattice specific heat) and K_a (lattice thermal conductivity) parameters in the second equation differ, depending on the material. In this study on boron carbide, their values have been taken from an IAEA report [35]. The thermal conductivity decreases from 30 $W{\cdot}K^{-1}{\cdot}m^{-1}$ at 300 K to 10 $W{\cdot}K^{-1}{\cdot}m^{-1}$ at 2600 K. The heat capacity increases from 1 kJ K^{-1} kg^{-1} at 300 K to 4.5 $kJ{\cdot}K^{-1}{\cdot}kg^{-1}$ at 2600 K.

For insulators, the key parameter is the electron / lattice interaction mean free path (λ) which is directly inversely linked to the electron/phonon coupling $g(T_e - T_a)$ by Eq. (3).

$$g(T_e - T_a) = \frac{D_e.C_e}{\lambda^2} \quad (3)$$

With: $C_e = 1$ J·$(cm^3{\cdot}K)^{-1}$ and $D_e = 2$ $cm^2{\cdot}s^{-1}$ assuming that the electronic heat capacity (C_e) is temperature independent, such as hot electrons in metals. D_e stands for the electronic thermal diffusivity. Values of D_e and C_e are taken according to the paper of Toulemonde et al. [36].

We calculated λ for boron carbide, thanks to Eq. (4) taken from [37].

$$\lambda = \lambda_0 + A.e^{-\frac{E_g}{E_1}} \quad (4)$$

With the following constants determined by Quentin [37]: $\lambda_0 = 4.15$ nm, $A = 8.66$ nm and $E_1 = 1.14$ eV. E_g is the gap energy of the considered insulator.

B_4C is an insulator material whose gap is not determined with accuracy but most studies [38–39] give values between 3 eV and 4 eV. Therefore, we determined that λ ranged from 4.4 nm to 4.7 nm. Thereafter, we assume a value of 4.5 nm in all calculations presented in this paper.

A(r,t) and B(r,t) correspond to the distribution functions of the incident ion energy deposition to the electronic sub-system and to the lattice sub-system respectively. They can be expressed (Eq. (5) and Eq. (6)) thanks to the formalism proposed by Waligorski et al. [40] and by Mieskes et al. [41].

$$A(r,t) = f(r).u(t) \quad (5)$$

With: $\int f(r)\ 2\pi\ r\ dr = S_e$

And, u(t) being a normalized Gaussian law.

$$B(r,t) = k.\frac{e^{-\frac{r}{r_0}}}{r}.u(t) \quad (6)$$

With: $\int k\ \frac{e^{-\frac{r}{r_0}}}{r}\ 2\pi\ r\ dr = S_n$

And: r_0 the radius of the cylinder where the nuclear energy is deposited (around 1 nm as it can been found in the literature [42]).

The aim of this calculation is to evaluate if the deposited energy after irradiation overcomes the melting energy of B_4C. This value is evaluated to 0.85 eV at^{-1} by adding the melting latent enthalpy taken from reference [43] and the enthalpy ΔH at melting temperature calculated with the equation of Shomate (Eq. (7)) along with the coefficients (A to H) determined by Chase [44] for B_4C.

$$\Delta H = H_T - H_{298K} = A.T + \frac{B\ T^2}{2} + \frac{C\ T^3}{3} + \frac{D\ T^4}{4} - \frac{E}{T} + F - H \quad (7)$$

With $T = t$ (in K) / 1000.

4.2. Results obtained with the iTS model

Let us now consider the deposited energy at the surface. The evolution of the deposited ion energy all along its track was calculated thanks to the iTS model. Fig. 6 presents the calculation results obtained for irradiation with sulfur ions at 100 MeV (Fig. 6.a) and iodine ions respectively at 60 (Fig. 6.b) and 100 MeV (Fig. 6.c). The calculations have been made in three modes: (i) with S_e only ($S_n = 0$), (ii) with S_n only ($S_e = 0$) and, (iii) with both S_e and S_n.

For sulfur ions, calculations show that the energy at the surface remains below 0.18 eV at^{-1}, namely below 1200 K. As expected, the contribution of S_n is negligible and the energy comes from S_e only. The irradiation with sulfur ions does not produce any dpa at the surface, as the energy loss regime is purely electronic. Therefore, no modification of the structure is expected with these irradiation conditions.

For iodine ions, the graphs corresponding to the calculation mode with both S_n and S_e show that the melting energy is reached (0.85 eV at^{-1}) within a cylinder with a radius of 0.5 nm for the irradiation at 60 MeV and with a radius of 0.6 nm for the irradiation at 100 MeV. If we consider calculations carried out with S_e only or with S_n only, we can observe that the melting energy is never reached for the 60 MeV energy irradiation and is barely reached for the 100 MeV energy irradiation. This result was expected for the S_n contribution because only a maximum of 0.2 dpa (calculated by SRIM) is created at the surface for both irradiation energies. The literature [14] shows the occurrence of an amorphization threshold, induced by collision cascades, around 3 dpa. In our irradiation conditions, the induced dpa values are 30 times lower. Thus, amorphization cannot be assigned to collision cascades only. This clearly shows a synergic effect between S_n and S_e (let us remind that we are in a mixed irradiation regime) which allows to exceed the melting energy. This effect was already observed by Toulemonde et al. in silicon irradiated with Gold ions at 4.8 and 9.8 MeV [45].

The calculations presented in Fig. 6 also show that the thermal spike lasts less than 10^{-11} s. It suggests that a quenching process occurs after the local melting inside the track of each incident ion.

5. Discussion

The combination of Raman spectroscopy and Microscopy (SEM and TEM) shows clearly a full amorphization of the B_4C sample surfaces irradiated with iodine ions as no order can be found at intermediate or long range with these techniques. The iTS model indicates that the amorphization is induced by local melting on the incident ion path. This melting-quenching process, induced by SHI and producing an amorphous phase inside the ion track, was already observed for instance, in $LiNbO_3$ by Szenes [46]. The iTS model predicts that the radius of the produced latent tracks is very small in B_4C in comparison with the usual ~10 nm found in other

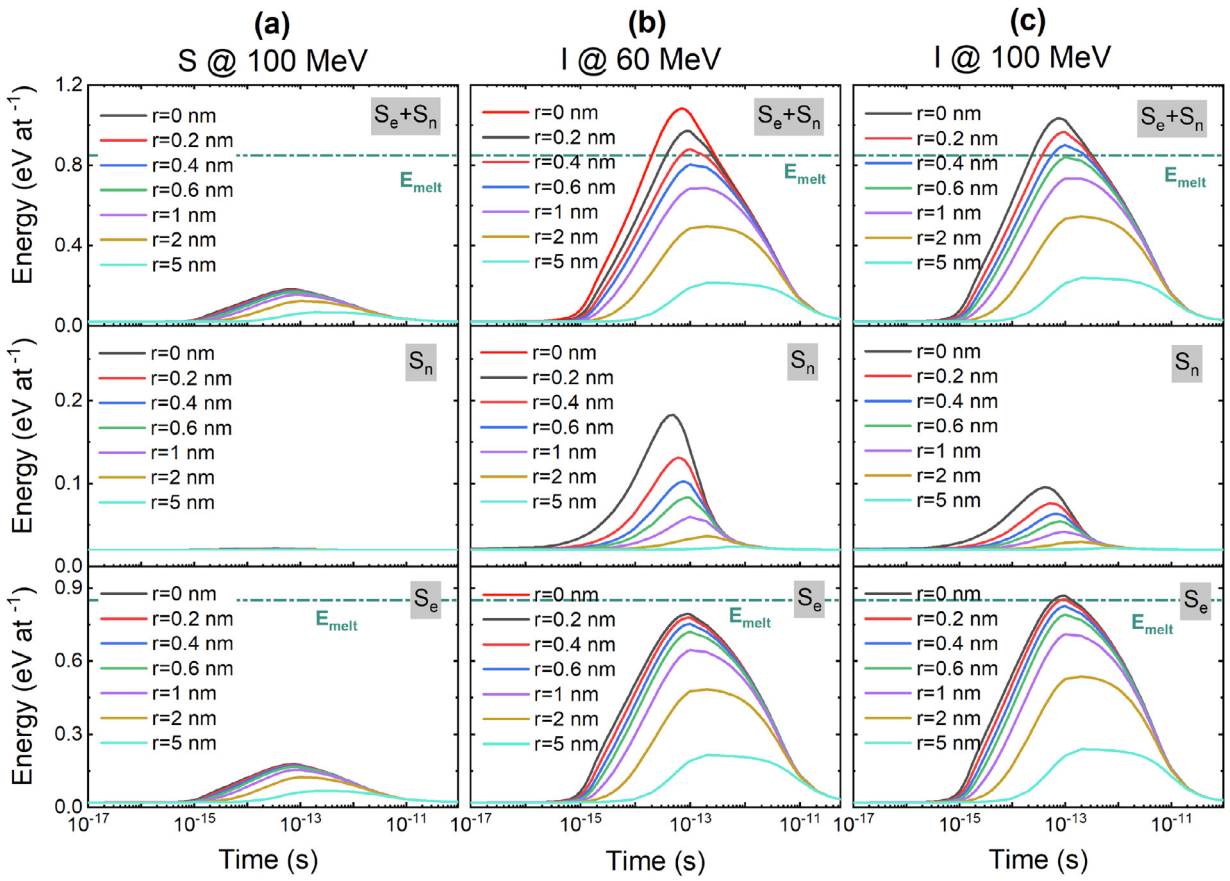

Fig. 6. *Deposited energy at the surface within a cylinder of different radius, calculated from the iTS Model, relative to sulfur irradiation at 100 MeV (a) and iodine irradiation at 60 MeV (b) and 100 MeV (c). The* B_4C *melting energy* E_{melt} *is indicated by a dash-dot line.*

materials but rather close to the one found in Highly Oriented Pyrolytic Graphite (around 2 nm) which is one of the smallest [47]. Even if the fluence is quite high in our irradiation experiments, it is mandatory to verify if the complete amorphization of the surface can be explained by an overlap model. This kind of model considers the overlapping of the amorphized regions created along each individual ion path. Therefore, the amorphization area grows with the irradiation fluence and the kinetics of the amorphization area S is generally associated with an Avrami-like (sigmoidal) law as expressed in Eq. (8):

$$S = 1 - \exp\left\{-\left(\frac{\phi}{\phi_0}\right)^n\right\} \tag{8}$$

With: ϕ, the fluence at a given irradiation time; ϕ_0 and n two adjustable parameters.

Obtaining the values of the two adjustable parameters would require a lot of irradiated samples and a specific study, which is not the purpose of this paper. However, we can rely on the work of Garcia et al. [48] who have developed a physical model for electronic excitation induced amorphization. They consider that each "swift" incident ion generates initially a full amorphous core and a defective region (called a halo) which can interact with other defective regions to increase the total amorphization area. They propose several values for n and ϕ_0 depending on different physical regimes and on the cross-section of the core and of the halo which can be basically approximated by their surfaces. In this paper, we have considered that the full amorphous core inside each ion track consists in a disk with a 0.55 nm radius (the iTs calculations show that melting occurs when the radius reaches 0.6 nm and 0.5 nm for the irradiations performed at 100 and 60 MeV respectively). We obtained values ranging from 1.05 to 1.35 for the parameter n and values ranging from 3.3×10^{13} at·cm^{-2} to 9.2×10^{13} at·cm^{-2} for the parameter ϕ_0. Thanks to Eq. (8), we can calculate that the amorphization area S exceeds 97% in our irradiation conditions for all the {n; ϕ_0} sets. This is in agreement with our experimental results showing a total amorphization of the surface even if the calculated radii of the tracks formed by SHI are small.

Agullo-Lopez et al. [49] have also highlighted the "memory effect" after the passage of a swift heavy ion. They showed that the fluence required to amorphize an insulator could be decreased when the electronic stopping power is increased and reciprocally. In our experiment, we have seen that when depth increases (which means a decrease of the S_e value), the amorphized part of the total area decreases as it has been shown in Fig. 5. It is clear that an electronic stopping power threshold is required to initiate the amorphization process for our irradiation fluence. In order to determine this threshold occurrence, we have represented in Fig. 7, both the evolution of the electronic (S_e) and nuclear (S_n) stopping powers *versus* depth, and opposite, the Raman mapping for the 60 MeV and 100 MeV iodine irradiated samples. The analysis was made on the cross-section of the samples irradiated with iodine ions. The Raman mapping displayed on Fig. 7a) is the same than Fig. 4 but in two dimensions for the sake of more clarity. We can estimate from Fig. 7a) that S_e value around 8.5 ± 0.5 keV·nm^{-1} is the limit value at which a Raman signal can be observed (around 3 µm with an uncertainty of 0.4 µm taking into account the spatial resolution of the laser beam), for 60 MeV iodine ion irradiation. Now, if we take a 2.5 µm value according to the TEM results, we find a S_e value around 9 keV·nm^{-1}. For the irradiation with 100 MeV iodine ions, the same procedure leads to a S_e threshold

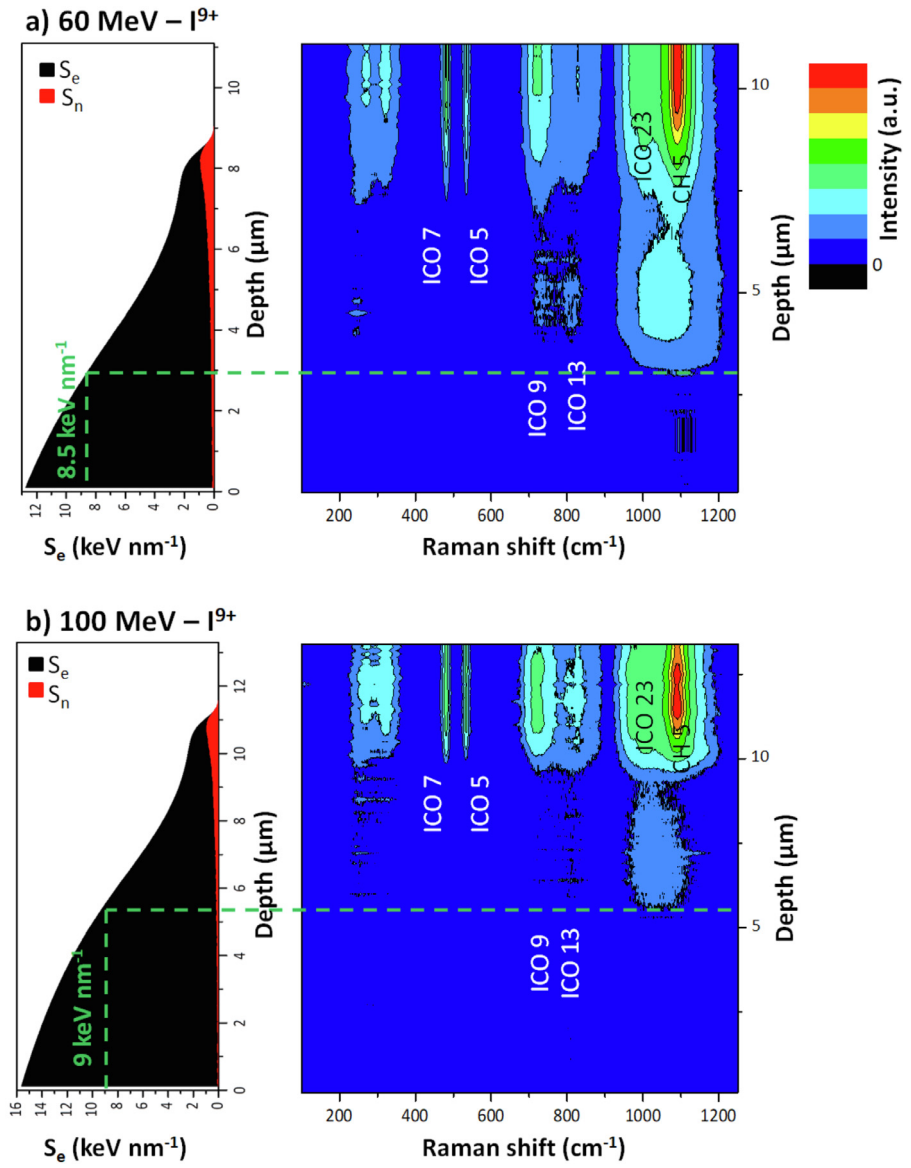

Fig. 7. *Comparison of the evolution of S_n and S_e as a function of depth (on the left) with 2D Raman mapping (on the right) for (a) 60 MeV and (b) 100 MeV iodine irradiations of* B_4C. *The dashed line put forwards the S_e amorphization threshold.*

of around 9 keV nm^{-1}. This threshold value could be impacted by the S_n value which is low but not null in our experiments. There could be some synergic effect between S_e&S_n as it is suggested by the iTS model and as it was shown by Hooda et al. [50] who have performed irradiation of germanium with 100 MeV Ag ions ($S_e = 16.5$ keV·nm^{-1} and $S_n = 0.1$ keV·nm^{-1} at the sample surface). Other irradiation experiments should be required to consolidate the threshold value proposed in this paper.

This value determined in B_4C is of the same order of magnitude but higher than the one found in HOPG (Highly Oriented Pyrolytic Graphite). Indeed, from scanning transmission microscopy (STM) investigations of SHI-irradiated HOPG, Liu et al. have proposed a track formation threshold at a S_e value of 7.3 ± 1.5 keV·nm^{-1} [47].

Lastly, the charge of the incident ions should be taken into account. Indeed it has been shown that irradiation with Highly Charged Ions (HCIs) has the same effect than SHI even at lower energies [51–52]. The main difference between HCI and SHI is that the deposited energy is located in a very small volume at the sample surface for the HCIs. As the iodine charge is 9+, this effect could also play a role but a minor one as few changes are expected for charges below 10+ according to [51–52].

Hence, in order to determine an accurate amorphization threshold (for S_e and S_n), it would be necessary to perform irradiations at higher energies (in order to decrease S_n) and lower fluences (to limit the interactions of two latent tracks). These irradiations will also help to clarify the value of the electron/lattice interaction mean free path (λ) which is critical in the iTS calculations for semi-conductors as it was pointed out by Sall et al. [53] especially to determine the radius of latent tracks.

6. Conclusions

In this paper, we have studied the structural modifications induced in B_4C by swift heavy ion irradiation, by using Raman mapping and electronic microscopy (SEM, TEM). Considering the large ion range, it was possible to perform successfully the Raman ex-

periments on the sample edges. The main following conclusions can be drawn:

1) The effects of pure electronic excitations below 4.1 keV·nm^{-1} do not modify the structure of B_4C. This indicates that, in reactor conditions, this effect solely has no chance to damage the B_4C structure.
2) B_4C has been amorphized with different heavy ions at relative high velocities corresponding to electronic stopping powers S_e of 12 and 15 keV·nm^{-1} (values at the sample surface) thanks to the synergy between collisions cascades and electronic excitations.
3) The iTS model has been successfully applied to explain the amorphization of the material through a melting-quenching process occurring in the incident ion track. The irradiation fluences (3×10^{15} at·cm^{-2} and 5×10^{15} at·cm^{-2}) were high enough for the total surface amorphization.
4) An amorphization threshold has been determined for a S_e value around 9 keV·nm^{-1}. This value can be slightly impacted by two parameters, which are the nuclear stopping power, even if it is small as in our experiments, and the charge of the incident ion (Highly Charged Ions).

Declaration of Competing Interest

The authors declare that they have no known competing financial interests or personal relationships that could have appeared to influence the work reported in this paper..

Acknowledgments

This work was supported by the CNRS NEEDS program within the MATABS project. The authors are very grateful to the Tandem-Orsay accelerator staff during ion irradiation experiments. The access to the JEOL2010F microscope and the Zeiss NVision40 FIB/SEM was provided by the CLYM (center Lyonnais de Microscopie: www.clym.fr) supported by the CNRS, the "GrandLyon" and the Rhône-Alpes Region (France).

Supplementary materials

Supplementary material associated with this article can be found, in the online version, at doi:10.1016/j.jnucmat.2020.152737.

References

[1] A Technology Roadmap For Generation IV Nuclear Energy Systems, U.S. Department of Energy, December 2002 GIF-002-00.
[2] K. Aoto, P. Dufour, H.Y. Yang, J.P. Glatz, Y. Kim, Y. Ashurko, R. Hill, N. Uto, A summary of sodium-cooled fast reactor development, Prog. Nucl. Energ. 77 (2014) 247–265, doi:10.1016/j.pnucene.2014.05.008.
[3] F. Gauché, Generation IV reactors and the ASTRID prototype: lessons from the Fukushima accidentL, C.R. Physique 13 (2012) 365–371, doi:10.1016/j.crhy.2012.03.004.
[4] K.H.G. Ashbee, Defects in boron carbide before and after neutron irradiation, Acta Metall. 19 (1971) 1079–1085, doi:10.1016/0001-6160(71)90040-X.
[5] G.L. Copeland, W.R. Martin, R.G. Donnelly, Irradiation Behavior of Boron Carbide, Nucl. Technol. 16 (1972) 226–237, doi:10.13182/NT72-A31189.
[6] A. Jostsons, C.K.H. Dubose, Microstructure of boron carbide after fast neutron irradiation, J. Nucl. Mater. 44 (1972) 91–95, doi:10.1016/0022-3115(72)90134-1.
[7] K. Froment, D. Gosset, M. Guery, B. Kryger, C. Verdeau, Neutron irradiation effects in boron carbides: evolution of microstructure and thermal properties, J. Nucl. Mater. 188 (1992) 185–188, doi:10.1016/0022-3115(92)90468-Z.
[8] T. Maruyama, S. Onose, T. Kaito, H. Horiuchi, Effect of Fast Neutron Irradiation on the Properties of Boron Carbide Pellet, J. Nucl. Sci. Tech. 34 (1997) 1006–1014, doi:10.1080/18811248.1997.9733777.
[9] D. Simeone, D. Gosset, D. Quirion, X. Deschanels, Study of B_4C microstructure evolution under neutron irradiation by X-ray diffraction profiles analysis, J. Nucl. Mater. 264 (1999) 295–308, doi:10.1016/S0022-3115(98)00485-1.
[10] D. Simeone, C. Mallet, P. Dubuisson, G. Baldinozzi, C. Gervais, C.J. Maquet, Study of boron carbide evolution under neutron irradiation byRaman spectroscopy, J. Nucl. Mater. 277 (2000) 1–10.
[11] D. Gosset, B. Provot, Boron carbide as a potential inert matrix: an evaluation, Prog. Nucl. Energ. 38 (2001) 263–266, doi:10.1016/S0149-1970(00)00113-X.
[12] R. Lazzari, N. Vast, J.M. Besson, S. Baroni, A. Dal Corso, Atomic Structure and Vibrational Properties of Icosahedral B_4C Boron Carbide, Phys. Rev. Lett. 83 (1999) 3230–3233, doi:10.1103/PhysRevLett.83.3230.
[13] D. Lee, P.J. Bray, T.L. Aselage, The NQR and NMR studies of icosahedral borides, J. Phys. Condens. Mat. 11 (1999) 4435–4450, doi:10.1088/0953-8984/11/22/314.
[14] D. Gosset, S. Miro, S. Doriot, G. Victor, V. Motte, Evidence of amorphisation of B_4C boron carbide under slow, heavy ion irradiation, Nucl. Instr. Meth. Phys. Res. B 365 (2015) 300–304, doi:10.1016/j.nimb.2015.07.054.
[15] D. Gosset, S. Miro, S. Doriot, N. Moncoffre, Amorphisation of boron carbide under slow heavy ion irradiation, J. Nucl. Mater. (2016), doi:10.1016/j.jnucmat.2016.04.030.
[16] G. Victor, Y. Pipon, N. Moncoffre, N. Bérerd, C. Esnouf, T. Douillard, A. Gentils, In situ TEM observations of ion irradiation damage in boron carbide, J. Europ. Ceram. Soc. 39 (2019) 726–734, doi:10.1016/j.jeurceramsoc.2018.11.011.
[17] H.M.H. Inui, H. Mow, H. Fujita, Electron irradiation induced crystalline-amorphous transition in ceramics, Acta. Metall 37 (1989) 1337–1342, doi:10.1016/0001-6160(89)90163-6.
[18] H. Mori, T. Sakata, H. Inui, High-resolution electron microscope studies of irradiation-induced crystalline-to-amorphous transition in boron carbide, Phil. Mag. Lett. 61 (1990) 49–53, doi:10.1080/09500839008206479.
[19] T. Maruyama, M. Iwanami, S. Ohnuki, T. Suda, S. Watanabe, K. Ikezawa, Effects of Radiation on Materials, in: 21st International Symposium; Book Series, 1447, American Society For Testing And Materials Special Technical Publication, 2004, pp. 670–679.
[20] M.N. Mirzayev, E. Demir, K.F. Mammadov, et al., Amorphisation of boron carbide under gamma irradiation, Pramana-J. Phys. 94 (2020) 110, doi:10.1007/s12043-020-01980-3.
[21] G. Victor, Y. Pipon, N. Bérerd, N. Toulhoat, N. Moncoffre, N. Djourelov, S. Miro, J. Baillet, N. Pradeilles, O. Rapaud, A. Maître, D. Gosset, Structural modifications induced by ion irradiation and temperature in boron carbide B_4C, Nucl. Instr. Meth. Phys. Res. B 365 (2015) 30–34, doi:10.1016/j.nimb.2015.07.082.
[22] L. Roumiguier, A. Jankowiak, N. Pradeilles, G. Antou, A. Maître, Mechanical properties of submicronic and nanometric boron carbides obtained by Spark Plasma Sintering: influence of B/C ratio and oxygen content, Ceram. Int. 45 (2019) 9912–9918, doi:10.1016/j.ceramint.2019.02.033.
[23] F. Réjasse, M. Georges, N. Pradeilles, G. Antou, A. Maître, Experimental investigation and thermodynamic evaluation of the C–Hf–O ternary system, J. Am. Ceram. Soc. 101 (2018) 3367–3772, doi:10.1111/jace.14901.
[24] R. Belon, G. Antou, N. Pradeilles, A. Maître, D. Gosset, Mechanical behaviour at high temperature of spark plasma sintered boron carbide ceramics, Ceram. Int. 43 (2017) 6631–6635, doi:10.1016/j.ceramint.2017.02.053.
[25] B. Marchand, N. Moncoffre, Y. Pipon, N. Bérerd, C. Garnier, L. Raimbault, P. Sainsot, T. Epicier, C. Delafoy, M. Fraczkiewicz, C. Gaillard, N. Toulhoat, A. Perrat-Mabilon, C. Peaucelle, Xenon migration in UO_2 under irradiation studied by SIMS profilometry, J. Nucl. Mater. 440 (2013) 562–567, doi:10.1016/j.jnucmat.2013.04.005.
[26] J.F. Ziegler, M.D. Ziegler, J.P. Biersack, SRIM – The Stopping and range of ions in matter (2010), Nucl. Instr. Meth. Phys. Res. B 268 (2010) 1818–1823, doi:10.1016/j.nimb.2010.02.091.
[27] L. Thomé, S. Moll, J. Jagielski, A. Debelle, F. Garrido, G. Sattonnay, Damage Accumulation in Nuclear Ceramics, in: VIII International Conference ION 2010, Kazimierz Dolny, Poland, 2010, pp. 7–12.
[28] C. Trautmann, Modifications induced by swift heavy ions, Bull. Mater. Sci. 22 (1999) 679–686.
[29] S. Miro, E. Bordas, L. Thome, J.M. Costantini, F. Lepretre, P. Trocellier, Y. Serruys, L. Beck, D. Gosset, R. Verlet, J. Huguet-Garcia, M. Tupin, M. Belleil, Monitoring of the microstructure of ion-irradiated nuclear ceramics by *in situ* Raman spectroscopy, J. Raman Spectrosc. 47 (2016) 476–485, doi:10.1002/jrs.4837.
[30] N. Vast, R. Lazzari, J.M. Besson, S. Baroni, A. Dal Corso, Atomic structure and vibrational properties of icosahedral α-boron and B_4C boron carbide, Comput. Mater. Sci. 17 (2000) 127–132, doi:10.1016/S0927-0256(00)00009-4.
[31] A. Jay, PhD thesis, Ecole Polytechnique, Université Paris-Saclay, France, 2015.
[32] C. Pallier, PhD thesis, Université Bordeaux 1, France, 2012.
[33] Ech. Silk, R.R. Barnes, Examination of fission fragment tracks with an electron microscope, Philos. Mag. 4 (1959) 970–972, doi:10.1080/14786435908238273.
[34] M. Toulemonde, E. Paumier, C. Dufour, Thermal spike model in the electronic stopping power regime, Radiat. Eff. Defect S. 126 (1993) 201–206, doi:10.1080/10420159308219709.
[35] IAEA – TECDOC-949 (1997) « Thermophysical properties of materials for water cooled reactors ».
[36] M. Toulemonde, Ch. Dufour, A. Meftah, E. Paumier, Transient thermal processes in heavy ion irradiation of crystalline inorganic insulators, Nucl. Instr. Meth. Phys. Res. B 166-167 (2000) 903–912, doi:10.1016/S0168-583X(99)00799-5.
[37] A. Quentin, PhD thesis, Université de Caen, 2010.
[38] F. Mauri, N. Vast, C.J. Pickard, Atomic Structure of Icosahedral B_4C Boron Carbide from a First Principles Analysis of NMR Spectra, Phys. Rev. Lett. 87 (2001) 085506, doi:10.1103/PhysRevLett.87.085506.
[39] D.R. Armstrong, J. Bolland, P.G. Perkins, G. Will, A. Kirfel, The nature of the chemical bonding in boron carbide. IV. Electronic band structure of boron carbide, $B_{13}C_2$, and three models of the structure $B_{12}C_3$, Acta Cryst. B 39 (1983) 324–329, doi:10.1107/S0108768183002487.

[40] M.P.R. Waligorski, R.N. Hamm, R. Katz, The Radial Distribution of Dose around the Path of a Heavy Ion in Liquid Wate, Nucl. *Tracks Radiat. Meas.* 11 (1986) 309–319.
[41] H.D. Mieskes, W. Assmann, F. Grüner, H. Kucal, Z.G. Wang, M. Toulemonde, Electronic and nuclear thermal spike effects in sputtering of metals with energetic heavy ions, Phys. Rev. B 67 (2003) 155414, doi:10.1103/PhysRevB.67.155414.
[42] E. Balanzat, S. Bouffard, Solid State Phenomena 30-31 (1993) 7–74.
[43] E.S. Domalski, the heat of formation of boron carbide, J. Res. Nat. Bur. Nat. U.S. 72A (1968) 33.
[44] M.W. Chase Jr, NIST-JANAF Themochemical Tables, Fourth Edition, J. Phys. Chem. Ref. Data, Monograph 9 (1998) 1–1951.
[45] M. Toulemonde, W.J. Weber, G. Li, V. Shutthanandan, P. Kluth, T. Yang, Y. Wang, Y. Zhang, Synergy of nuclear and electronic energy losses in ion-irradiation processes: the case of vitreous silicon dioxide, Phys. Rev. B 83 (2011) 054106, doi:10.1103/PhysRevB.83.054106.
[46] G. Szenes, Amorphous tracks in insulators induced by monoatomic and cluster ions, Phys. Rev. B 60 (1999) 3140, doi:10.1103/PhysRevB.60.3140.
[47] J. Liu, R. Neumann, C. Trautmann, Tracks of swift heavy ions in graphite studied by scanning tunneling microscopy, Phys. Rev. B 64 (2001) 184115, doi:10.1103/PhysRevB.64.184115.
[48] G. García, A. Rivera, M.L. Crespillo, N. Gordillo, J. Olivares, F. Agulló-López, Amorphization kinetics under swift heavy ion irradiation: a cumulative overlapping-track approach, Nucl. Instr. Meth. Phys. Res. B 269 (2011) 492–497, doi:10.1016/j.nimb.2010.12.073.
[49] F. Agulló-López, G. García, J. Olivares, Lattice preamorphization by ion irradiation: fluence dependence of the electronic stopping power threshold for amorphization, J. Appl. Phys. 97 (2005) 093514, doi:10.1063/1.1896444.
[50] S. Hooda, S.A. Khan, B. Satpati, D. Kanjilal, D. Kabiraj, Thermal spike effect in sputtering of porous germanium to form surface pattern by high energy heavy ions irradiation, Appl. Phys. Lett. 108 (2016) 201603, doi:10.1063/1.4950710.
[51] F. Aumayr, S. Facsko, A.S. El-Said, C. Trautmann, M. Schleberger, J. Phys.: Condens. Matter 23 (2011) 393001, doi:10.1088/0953-8984/23/39/393001.
[52] S. Facsko, R. Heller, A.S. El-Said, W. Meissl, F. Aumayr, J. Phys.: Condens. Matter 21 (2009) 224012, doi:10.1088/0953-8984/21/22/224012.
[53] M. Sall, I. Monnet, F. Moisy, C. Grygiel, S. Jublot-Leclerc, S. Della-Negra, M. Toulemonde, E. Balanzat, Track formation in III-N semiconductors irradiated by swift heavy ions and fullerene and re-evaluation of the inelastic thermal spike model, J. Mater. Sci. 50 (2015) 5214–5227, doi:10.1007/s10853-015-9069-y.